Smart Structures and Systems, *Vol. 34, No. 3 (2024) 145-156*
https://doi.org/10.12989/sss.2024.34.3.145

An assembled arc-shaped pendulum TMD with constant eddy current damping for structural vibration control

Shuli Wei [1,2a], Jian Wang [3b] and Jinping Ou*[1,2,3]

[1] *School of Civil and Environment Engineering, Harbin Institute of Technology (Shenzhen), Shenzhen 518055, China*
[2] *Shenzhen Key Laboratory of Intelligent Structure System in Civil Engineering, Shenzhen 518055, China*
[3] *Key Lab of Structures Dynamic Behavior and Control of the Ministry of Education, Harbin Institute of Technology, Harbin 150090, China*

(*Received November 9, 2022, Revised September 9, 2023, Accepted October 11, 2023*)

Abstract. Pendulum tuned mass damper with eddy current damping (EC-PTMD) is a promising TMD device for vibration control of structures. Previous study focused primarily on the plate-like configuration of EC-PTMD, which motion of inertial mass is approximately horizontal. However, uneven distribution of damping force, non-constant damping and low energy efficiency will be resulted. This study developed a newly assembled pendulum tuned mass damper with constant eddy current damping (AEC-PTMD) in the form of arc. The proposed AEC-PTMD consists of a rigid suspension with sufficient lateral stiffness to keep inertial mass motion in a plane, the conductor plate fixed on the baseplate, and arc-shaped back iron acted as inertial mass placed on two sides of conductor plate. Meanwhile, the arc-shaped permanent magnets (PMs) are embedded into both sides of back iron to overcome the normal attraction and enhance greater magnetic density. Based on the Biot-Savart Law, the analytical expressions of magnetic flux distribution for arc-shaped PM are derived and assessed. Meanwhile, the effect of ferromagnetic media on magnetic flux distribution of arc-shaped PM is analyzed, which utilized a parameterization formula for the distance from the surface of the PM to a point outside. Further, the 3D finite element model (FEM) of an AEC-PTMD unit is established to evaluate the accuracy of the analytical results. A prototype of the proposed AEC-PTMD unit has been fabricated and laboratory experiments are conducted for the purpose of validating analytical and FEM results. All of these results have a good agreement.

Keywords: arc-shaped permanent magnet; eddy current damping; pendulum tuned mass damper

1. Introduction

Mitigation of vibration of civil structures induced by earthquake and strong wind through structural vibration control, which can enhance the structural functionality and safety, is considered as a major breakthrough in civil engineering (Ou 2003, Korkmaz 2011, Amezquita-Sanchez *et al*. 2014). The traditional structural design approach only relies on changing the structure's own performance, such as changing the rigidity, damping, or the mass distribution of the structure to resist dynamic loads. Besides this way, the vibration control method can advance the traditional structural design approach to actively control the dynamic response of the structure (Wang and Lin 2015). A typical way is to reduce structural response of structures by installing damping devices, such as magnetorheological (MR) dampers, TMD and AMD etc., which has been widely applied for vibration control of newly-built or existing buildings, bridges and so on (Xu *et al*. 2014, Sun and Jahangiri 2018, Lenggana *et al*. 2021).

Tuned mass dampers (TMD) have been widely recognized as an effective method for reducing structural vibration due to their efficiency, reliability, and low maintenance cost (Nagarajaiah 2009, Domizio *et al*. 2015, Elias and Matsagar 2017). Among TMD types, pendulum tuned mass damper (PTMD) suspended by ropes is commonly used and relies on gravity to provide the required restoring force. The natural frequency of PTMD is determined by the curvature of pendulum motion (Matta 2019). However, determining the optimum frequency and damping ratio of a PTMD is not an easy task. Gerges and Vickery (2005) derived the optimum design formula for planar PTMDs aiming to minimize the displacement of the structure under wind and earthquake excitations. Additionally, Roffel *et al*. (2013) proposed the optimum design formula to minimize the acceleration of slender tall buildings with PTMD installed under wind excitation. Shi *et al*. (2017) developed an adaptive-passive variable PTMD, whose pendulum length can be adjusted by microcontroller to retune its natural frequency to consistent with the natural frequency of structure. Other researches (Contreras *et al*. 2014, Pasala and Nagarajaiah 2014) have also made significant contributions in the similar orientation, exploring the principles and applications of PTMDs extensively.

In terms of TMDs, vibration energy is dissipated through the damping. Various dampers are applied in TMDs to improve their dissipation capability, such as viscoelastic

*Corresponding author, Professor,
E-mail: oujinping163@163.com
[a] Ph.D. Student, E-mail: weishuli2020@163.com
[b] Associate Professor, E-mail: wangjiantx@hit.edu.cn

ISSN: 1738-1584 (Print), 1738-1991 (Online)

damper (Weber *et al*. 2011, Weber and Maslanka 2012), friction damper (Domenico and Ricciardi 2018) and eddy current damper (ECD) (Mehrtash and Khamesee 2013, Pluk *et al*. 2014) etc. In comparison, the ECD is an effective mechanism for suppressing vibration of dynamic systems. ECDs are designed based on the principle of electromagnetic induction, which has the attractive merit of no friction and no mechanical contact. Therefore, it does not induce undesired additional stiffness to the overall stiffness of the structures. Moreover, the eddy current damping is approximately linear at low speed and easily adjusted by altering the air gap between the PMs and conductor plate (Ao and Reynolds 2019, Li *et al*. 2019). Due to these merits, the damping mechanism via eddy currents has been widely reported by many researchers (Ebrahimi *et al*. 2009, Mohanta *et al*. 2017, Diez-Jimenez *et al*. 2019). Sodano *et al*. (2005) developed an eddy current damping system to suppress the vibration of a cantilever beam. Subsequently, Sodano and Inman (2008) developed an active ECD that controlling eddy current force by changing the strength of the magnetic field induced through current coil. Recently, Zhang *et al*. (2020) proposed a rotary ECD for vibration control. It has been proved that all aforementioned ECDs are effective in reducing vibration.

The combination of ECDs and TMDs has been found to be effective in suppressing structural vibration, and numerous studies have demonstrated the effectiveness and robustness of EC-TMDs (Niu *et al*. 2018, Zhong *et al*. 2022). EC-PTMDs have also been investigated, Wang *et al*. (2012) carried out the theoretical analysis and experimental investigation of a large-scale EC-PTMD, and then confirmed its reliability and feasibility in practical applications. Lu *et al*. (2016) performed laboratory and field tests on a reduced-scale EC-PTMD installed at the Shanghai Center Tower in China, demonstrating its strong endurance and linear damping. Numerical research indicated that it has a good effect on reducing vibration in structure response under wind and earthquake excitation. Wang *et al*. (2020) presented an adaptive-passive EC-PTMD, which can retune its frequency and the damping ratio by adjusting the air gap between PMs and conductor plate. The principle and application of EC-PTMDs have been studied and explored in all of these literatures. It should be noticed that these EC-PTMDs move approximately horizontal, which configuration is similar to the plate-like. However, the pendulum motion of EC-PTMDs may cause changes in the air gap between the PMs and the conductor plate, subsequently leading to fluctuations in eddy current damping. This will affect the effectiveness of the EC-PTMDs.

The purpose of this paper is to develop a novel assembled PTMD with constant eddy current damping (AEC-PTMD). The AEC-PTMD is constructed from standard units, which can be assembled to achieve a large damping capacity. Each unit comprises an arc-shaped mass block with PMs and arc-shaped conductor plate, where the PMs are arranged in a vertical arc embedded inside of the mass block and on both sides of the conductor plate. The curvature of the AEC-PTMD unit matches that of the pendulum's motion to ensure that the air gap between the PMs and conductor plate remains constant during operation, thus ensuring the eddy current damping maintains constant. In addition, the double-sided PM arrangement can overcome the normal attraction of the PMs to the conductor plate and allows for greater magnetic density.

In this paper, section 2 provides background on the need for AEC-PTMD development. Section 3 presents the configuration of the AEC-PTMD. Section 4 derives the analytical expressions of magnetic field distribution for special arc-shaped PM based on vector potential method. Section 5 characterizes the mechanical properties of the AEC-PTMD by using finite element method, meanwhile, parameters affecting its characteristics are analyzed. Finally, experimental results on an AEC-PTMD prototype are presented in Section 6, where the damping of AEC-PTMD is analyzed and compared to numeral results. Section 7 is a brief conclusion of the paper.

2. Analysis of EC-PTMD

2.1 Eddy current damping

Previous research (Zhu *et al*. 2019) has indicated that the calculation of eddy current damping and its interaction with original magnetic field are much complicated. To simplify the process of analysis and solution, some assumptions are made as follows:

- The magnetic field can be treated as a quasi-static field (Haus *et al*. 1989) and its distribution is uniform, ignoring effect of eddy current interaction with original magnetic field.
- The conductor plate always fully interacts with the magnetic field generated by PMs.
- The speed of inertial mass is always low, so that the eddy current damping is truly linear.
- The relative permeability of conductor plate and PM is 1, and conductivity of the conductor plate is constant. The magnetic conductivity of back iron is infinite, and its conductivity is ignored, *i.e*., its eddy current effect is not considered.

The damping force is calculated by the Lorentz force equation

$$F = \int J \times B \, dV \tag{1}$$

where dV represents the volume element in conductor. In addition, the current intensity inside the conductor is

$$J = \sigma(v \times B) \tag{2}$$

where σ is the electrical conductivity of the conductor, v is the velocity of the inertial mass relative to the conductor plate, and the magnetic field B is generated by PMs. In addition, a method of images in two dimensions on the electrostatic field solutions is needed when the size of the conductor is comparable to the dimensions of the source of the magnetic field (Zuo *et al*. 2011). Besides this method, a dimensionless coefficient G can be utilized to consider this

condition, which is proved to be simple and effective. The Eq. (1) can be described as

$$F_\theta = -GB^2tS\sigma v_\theta = -C_e v_\theta \tag{3}$$

where C_e is the eddy current damping coefficient and v_θ is the angular velocity of inertial mass. t, S are the thickness of conductor plate and the area of the magnetic field intersected by it, respectively. G can be calculated according to the reference (Zuo *et al*. 2011).

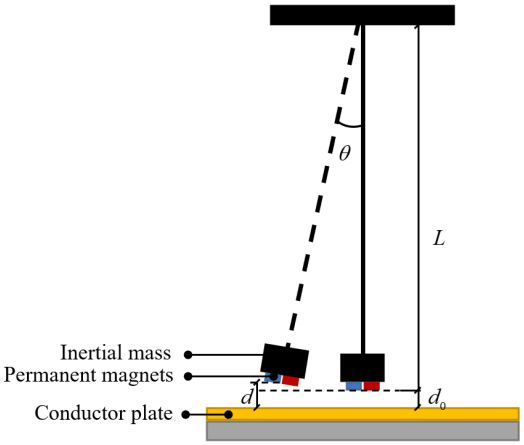

Fig. 1 Schematic diagram of pendulum Tuned mass damper with eddy current damping (EC-PTMD)

2.2 Effect of EC-PTMD pendulum motion on eddy current damping

Fig. 1 shows the sketch of a kind of pendulum tuned mass damper with eddy current damping (EC-PTMD). The PMs are attached to the mass block, and the conductor plate is fastened underneath it. The pendulum length of EC-PTMD is L and the air gap between PM and conductor plate is d. Once the magnetic and geometric parameters of PM are given, its magnetic field depends on the relative position between the selected point and the PM (Gou *et al*. 2004). For the swing motion in Fig. 1, the air gap represents such relative position. Consequently, it will affect the magnitude of the eddy current damping according to Eq. (3). As shown in Fig. 1, the air gap is varying when the EC-PTMD operated, therefore, its eddy current damping is not completely constant. The air gap can be written as

$$d = d_0 + L(1 - cos\,\theta) \tag{4}$$

where d_0 is the initial air gap and θ is the pendulum angle.

It is well known that only pendulum length L and pendulum angle θ could affect the magnitude of air gap. Assuming the pendulum length L_0 is the base-length, its corresponding eddy current damping C_0 is the baseline of the eddy current damping. The variation of the eddy current damping with the pendulum length and angle is illustrated in Fig. 2. It can be seen that the eddy current damping varies clearly. The contour map in Fig. 2(b) shows that the eddy current damping is decreased with the increasing of the pendulum length and angle, especially for larger pendulum length. When the pendulum length is 10 times of L_0, the resulting eddy current damping drops 30%

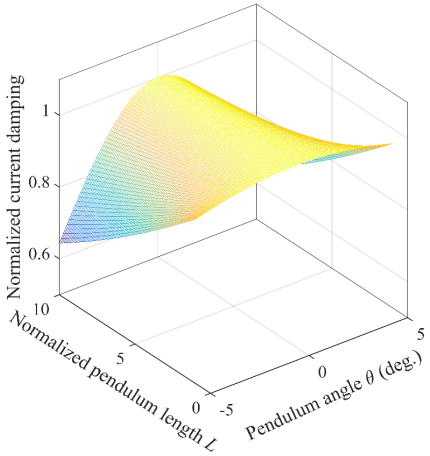

(a) 3D view for effect factors

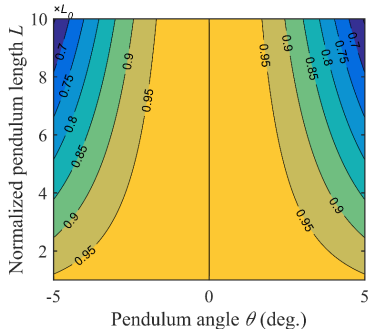

(b) Contour map

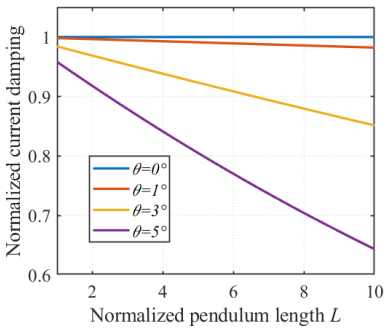

(c) Effect of pendulum length

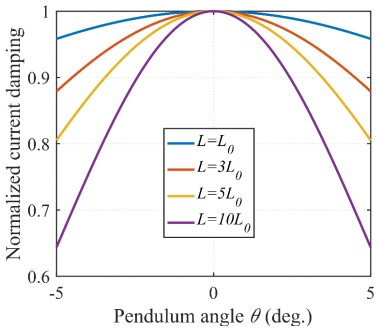

(d) Effect of pendulum angle

Fig. 2 Effect of pendulum length and angle of EC-PTMD on eddy current damping

comparing to the case with pendulum length L_0. In other words, the performance of EC-PTMD will be worse than expected. The reason of this phenomenon is that the increase of pendulum length and angle induces the bigger air gap, resulting in a reduction of the magnetic field on the conductor plate.

Furthermore, the relationship between eddy current damping and pendulum length in few fixed pendulum angles is given in Fig. 2(c). In Fig. 2(c), there is an approximately negative linear correlation between eddy current damping and pendulum length. Fig. 2(d) shows the relationship between eddy current damping and pendulum angle in few fixed pendulum lengths. It can be seen that the eddy current damping decreased while the pendulum angle increased. The relationship is almost quadratic.

In summary, the eddy current damping of the EC-PTMD with simple pendulum motion is not invariable, and its variation range depends on the pendulum length and angle.

3. Configuration and principle of the AEC-PTMD

Fig. 3 shows the configuration of the assembled pendulum tuned mass damper with constant eddy current damping (AEC-PTMD). The AEC-PTMD can be assembled by a number of standard units with designed eddy current damping. The unit is mainly composed of the inertial mass block with attached the permanent magnets (PMs) and

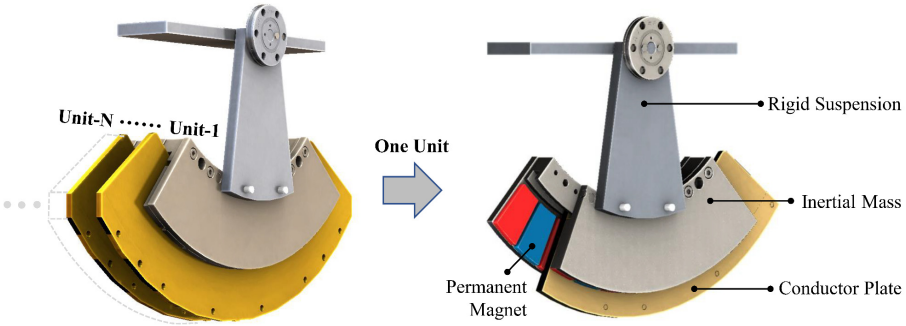

Fig. 3 Configuration of assembled pendulum Tuned mass damper with eddy current damping (AEC-PTMD)

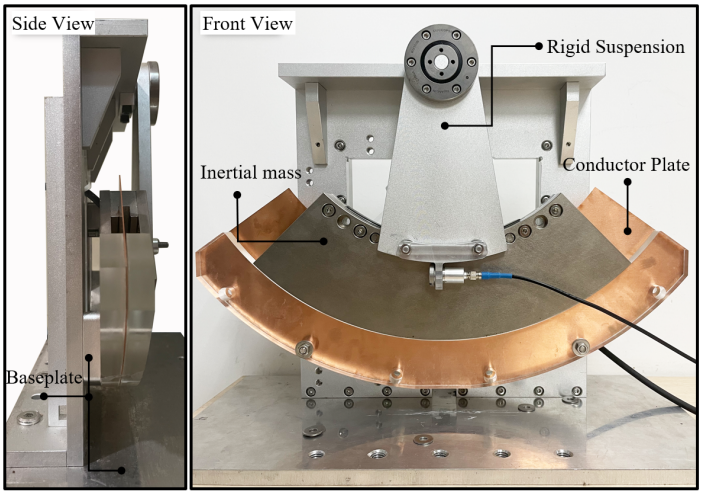

(a) Experimental prototype

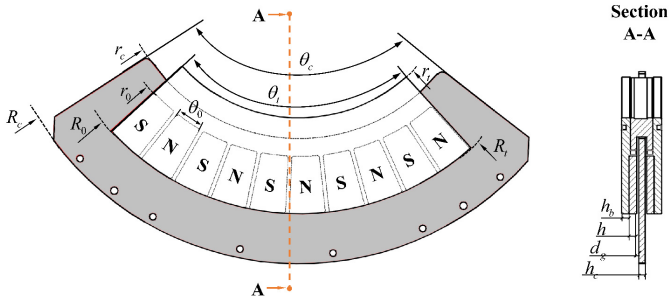

(b) Cross-section and geometric parameters of the prototype (Not to scale)

Fig. 4 Experimental prototype of the AEC-PTMD

Table 1 Geometrical and material parameters of the small-scaled prototype of AEC-PTMD

Item	Description	Value
PM	Inside radius, r_0	155 mm
	Outside radius, $R0$	200 mm
	Angle corresponding to arc-shaped, $\theta 0$	8°
	Thickness, h	6 mm
	Remanence, Br	1.29 T
Mass block	Mass, m_t	3.5 kg
	Inside radius, rt	125 mm
	Outside radius, Rt	200 mm
	Angle corresponding to the inertial mass block, θt	90°
	Thickness of the single side back iron, hb	6 mm
Conductor plate	Inside radius, r_c	140 mm
	Outside radius, Rc	240 mm
	Angle corresponding to the conductor plate, θc	110°
	Thickness, hc	0.1, 0.2, 0.5 mm
Suspension plate	Mass, ms	0.2 kg
	Radius, Rs	145 mm
Others	Air-gap length, dg	7.6 mm
	Angle corresponding to Pole length, θp	1°

conductor plate. The inertial mass block is suspended by a rigid suspension with sufficient stiffness to avoid the mass block rotate out of plane. Meanwhile, the conductor plate is fixed on the baseplate.

A small-scaled prototype of an AEC-PTMD unit designed and fabricated in laboratory for the purpose of characterization testing is given in Fig. 4. Meanwhile, its geometrical and material parameters are given in Table 1 and marked in Fig. 4(b). It is worth noting that the inertial mass block and conductor plate are designed as arc-shape, and the PMs are also designed as arc-shape to better fit on the mass block to make the magnetic flux uniformly distributed on the conductor plate. Additionally, in order to avoid the influence of normal force between conductor plate and PMs, PMs are symmetrically arranged on both sides of the conductor plate. The magnetization of PMs is perpendicular to the conductor plate, and the polarity of the adjacent PMs is opposite, which specific arrangement can be seen from Fig. 4(b). In this way, the eddy current damping force is evenly distributed on the mass block when the inertial mass block undergoes pendulum motion. Therefore, the eddy current damping induced by AEC-PTMD remains constant, and its magnitude is not influenced by the pendulum length and angle.

The working principle of the AEC-PTMD is to match the frequency of AEC-PTMD by selecting the appropriate parameters substantially with the natural frequency of structure. The absorbed energy of AEC-PTMD will be converted into heat and dissipated. The eddy current damping force will be generated as soon as the inertial mass block rotates along the conductor plate.

4. Theoretical basis of Magnetic field

4.1 Magnetic field characteristics of arc-shaped PM

As shown in the Eqs. (1)-(3), the eddy current damping is directly proportional to the square of the main magnetic field inside and outside the conductor plate. The layout and magnetic properties of PM must be designed to realize the desired magnetic field. In this section, depending on the assumption of electrodynamic molecule, the analytic expression of magnetic field distribution for special arc-shaped PM is derived using Biot-Savart Law. Cartesian coordinate (described in black) and cylindrical coordinate (described in red) in Fig. 5 are established simultaneously. $P(r,\theta,z)$ is a point out of PM while $Q(\hat{r},\hat{\theta},z_0)$ is a point on the surface of PM. Assuming that the direction of magnetization of PM is along axis z with a value of M_s, thereby the surface current density is

$$J_s = M_s = \frac{B_r}{\mu_0} \tag{5}$$

where B_r is the remanence of PM, and μ_0 is the permeability of vacuum, $\mu_0 = 4\pi \times 10^{-7} T \cdot \mathrm{m/A}$.

Selecting a thin current layer $A'B'C'D'A'$ with the thickness of dz_0, its current intensity can be described as $\boldsymbol{I} = J_s dz_0$. The magnetic field generated by current layer $A'B'C'D'A'$ at point $P(r,\theta,z)$ is dB, therefore, the total magnetic field can be expressed as

$$B = B_x i + B_y j + B_z k = \int_o^h dB_x i + dB_y j + dB_z k \tag{6}$$

where dB_x, dB_y, dB_zrepresent the components of magnetic field generated by the current layer at point P in the x, y and z directions, respectively. In this section, the magnetic field dB_z is taken as an example for analysis and derivation in the following. Furthermore, the magnetic field dB_z can be divided into four parts $(A'B', B'C', C'D', D'A')$ according to the superposition principle of magnetic field, which can be seen in Fig. 5. The yellow arrow represents the direction

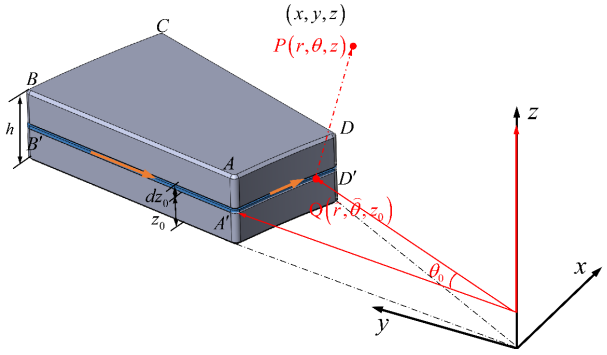

Fig. 5 Illustration of special arc-shaped PM

of the current on the current layer.

Taking the magnetic field generated by part $B'C'$ of PM as example. The current element can be calculated as

$$Idl_{BC} = J_s\left(-R_0\,\hat{sin}\,\theta\,i + R_0\,\hat{cos}\,\theta\,j + 0k\right)d\hat{\theta}dz_0 \tag{7}$$

The position vector $\overrightarrow{AP}$ can be written

$$\vec{r} = \left(r\cos\theta - R_0\,\hat{cos}\,\theta\right)i + \left(r\sin\theta - R_0\,\hat{sin}\,\theta\right)j + (z - z_0)k \tag{8}$$

According to Biot-Savart Law, the element of magnetic field $dB_z^{B'C'}$ along direction Z is

$$dB_z^{B'C'} = \frac{\mu_0}{4\pi}\oint\!\!\!\oint_S \frac{Idl_{BC}\times\vec{r}}{r^3} = \frac{\mu_0 J_s dz_0}{4\pi}\int_{\frac{\pi}{2}-\theta_0}^{\frac{\pi}{2}} \frac{R_0^2 - R_0 r\cos\left(\theta-\hat{\theta}\right)}{\left[\left(r\cos\theta - R_0\,\hat{cos}\,\theta\right)^2 + \left(r\sin\theta - R_0\,\hat{sin}\,\theta\right)^2 + (z-z_0)^2\right]^{3/2}}d\hat{\theta} \tag{9}$$

Using the same approach, the magnetic field at point P generated by other three parts is easily calculated. The magnetic field B_z at point P is derived as

$$\begin{aligned} B_z = {} & \frac{\mu_0 J_s}{4\pi}\int_0^h\int_{\frac{\pi}{2}-\theta_0}^{\frac{\pi}{2}}\left\{\frac{R_0^2 - R_0 r\cos\left(\theta-\hat{\theta}\right)}{\left[\left(r\cos\theta - R_0\,\hat{cos}\,\theta\right)^2 + \left(r\sin\theta - R_0\,\hat{sin}\,\theta\right)^2 + (z-z_0)^2\right]^{3/2}}\right. \\ & \left. - \frac{r_0^2 - r_0 r\cos\left(\theta-\hat{\theta}\right)}{\left[\left(r\cos\theta - r_0\,\hat{cos}\,\theta\right)^2 + \left(r\sin\theta - r_0\,\hat{sin}\,\theta\right)^2 + (z-z_0)^2\right]^{3/2}}\right\}d\hat{\theta}\,dz_0 \\ & + \frac{\mu_0 J_s}{4\pi}\int_0^h\int_{r_0}^{R_0}\left\{\frac{-r\cos(\theta+\theta_0)}{[(r\cos\theta - \hat{r}\sin\theta_0)^2 + (r\sin\theta - \hat{r}\cos\theta_0)^2 + (z-z_0)^2]^{3/2}}\right. \\ & \left. + \frac{r\cos\theta}{[(r\cos\theta)^2 + (r\sin\theta - \hat{r})^2 + (z-z_0)^2]^{3/2}}\right\}d\hat{r}\,dz_0 \end{aligned} \tag{10}$$

It should be noticed that the integrated function has no antiderivative at aforementioned formula, therefore, a discretization approach of integration is used to calculate magnetic flux density. Similarly, the magnetic flux density along axis x and y can be obtained.

COMSOL is a large-scale multi-physical field coupling analysis software that is based on finite element solutions of partial differential equations (groups) for the physical and engineering problems. AC/DC module in COMSOL can be used to understand, predict, and design electric and magnetic fields for steady-state, low-frequency, and transient applications. A finite element model of single PM is established by using AC/DC module to verify the accuracy of Eq. (10) and further explore the distribution of magnetic field of special arc-shaped PM. The PM parameters can be obtained from Table 1. Analytical results compared to finite element method (FEM) results are shown in Fig. 6, which show a good agreement between both. It proved the aforementioned analytical expressions are correct and accurate. Meanwhile, it can be seen that the magnetic field gradually decreases as the distance increases. In addition, Fig. 7 gives the magnetic field distribution at 1 mm upper the surface *ABCD* of the PM. The maximum magnetic field occurs at the edge of the PM, while in the middle it is slightly less than at the edge. Beyond the projected position of the PM, the magnitude of the magnetic field drops abruptly to zero.

Further, the analytical expressions for several arc-shaped PMs arranged along an arc according to the superposition principle can be derived using the coordinate

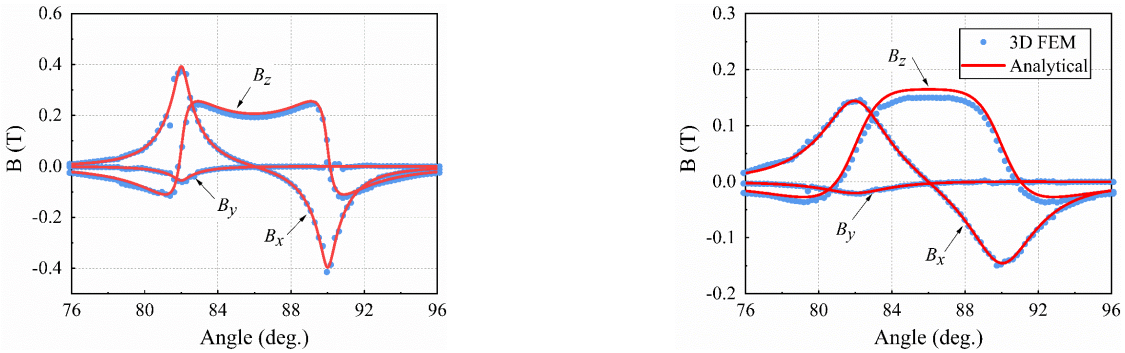

(a) Distance from point P to surface ABCD is 1 mm (b) Distance from point P to surface ABCD is 5 mm

Fig. 6 Comparison for magnetic field of single PM

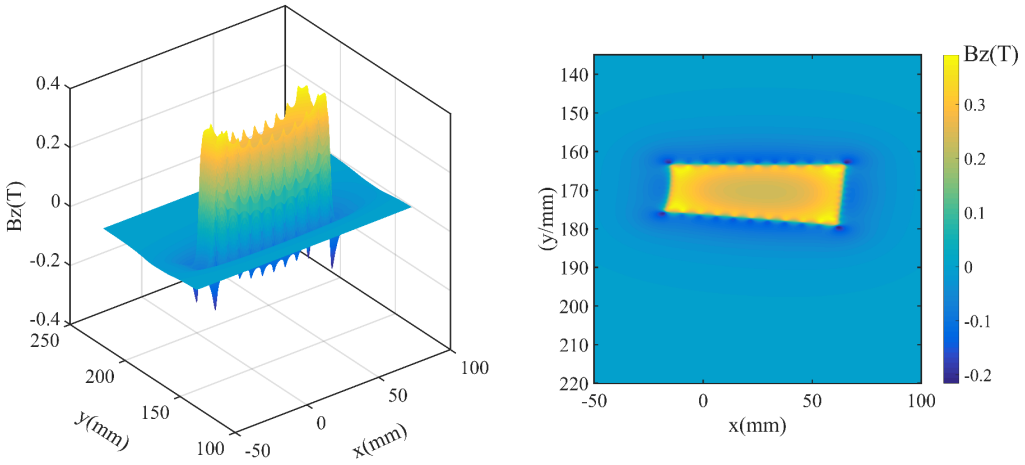

Fig. 7 3D diagram of magnetic field distribution of single PM

transformation approach. The analytical expressions can be written as follows

$$B_z = \sum_{i=1}^{n} sign(i) B_{zi}\left(\theta + (i-1)(\theta_0 + \theta_p)\right)$$
$$sign(i) = \begin{cases} 1 & mod\left(\frac{i}{2}\right) = 0 \\ -1 & mod\left(\frac{i}{2}\right) = 1 \end{cases} \quad (11)$$

where $\mathrm{sign}(i)$ represents the magnetization direction of PM, in this paper, the direction of magnetization along the positive Z-axis is assumed as positive.

4.2 Effect of the Ferromagnetic media

It should be noticed that the magnetic media (*i.e.*, back iron, which is made of ferromagnetic materials) in the magnetic field have a certain influence on the original magnetic field. The relationship between the total magnetic field B and the original magnetic field B_0 is usually linear, it can be expressed as

$$B = B' + B_0 = (1 + \chi_m) B_0 \quad (12)$$

where B' is induced magnetic field within the ferromagnetic material due to the original magnetic field and χ_m is magnetic susceptibility.

As shown in Fig. 4, the back iron is distributed on both sides of the PMs in this paper, both of which effects the magnetic field generated by PM. Its influence could not be neglected for analytical calculation. Consequently, it is essential to analyze the effects on the magnetic field from both sides of the device. This section includes separate examinations of the influence of back iron on the magnetic field for two scenarios: one where the PM is attached to a back iron (referred to as lower back iron), and the other involving a gap between the PM and back iron (referred to as upper back iron). The schematic diagram of these two situations is given in Fig. 8(a). As shown in Fig. 8(a), a simple finite element model (denoted as FEM-S) comprised is built, which consists of a PM and a back iron. Line A is a line between PM and upper back iron. Distance x_a and x_b are the distance from line A or back iron to the PM's urface, respectively. In order to intuitively demonstrate the impact of the back iron on the magnetic field, a cloud image of magnetic field modulus obtained from the FEM-S with

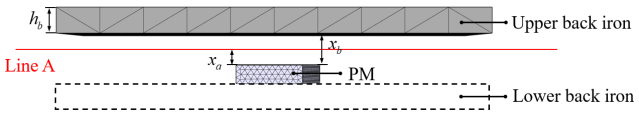

(a) Schematic diagram of FEM-S

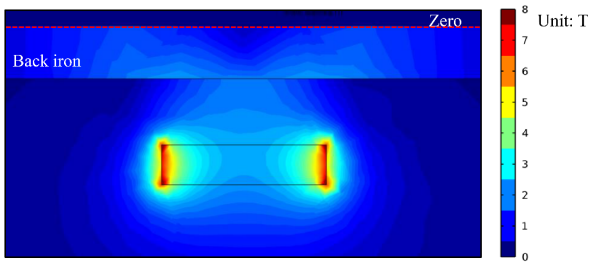

(b) Magnetic field cloud image resulted from the FEM-S with PM and upper back iron

Fig. 8 Schematic diagram of the FEM-S and its magnetic field cloud image

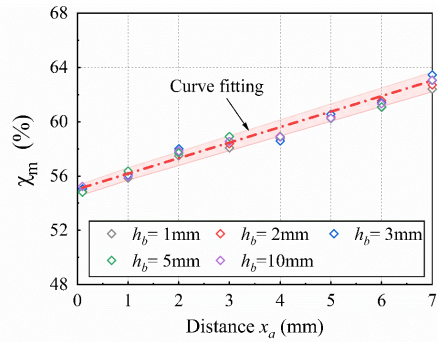

(a) Effect of lower back iron

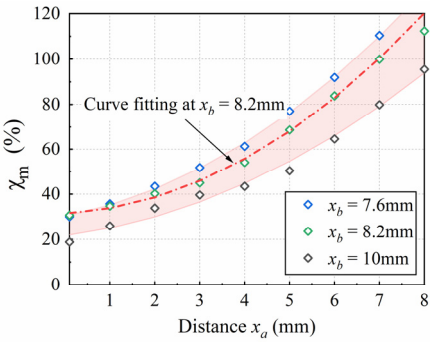

(b) Effect of upper back iron

Fig. 9 Effect of back iron on magnetic field of PM

s PM and upper back iron is presented in Fig. 8(b). The image clearly illustrates that the magnetic field is predominantly concentrated within the back iron and essentially nonexistent outside of it. This observation strongly suggests that the back iron effectively shields against magnetic leakage.

Furthermore, Fig. 9(a) illustrates the effect of the lower back iron on the magnetic susceptibility, as calculated by Eq. (12), where B and B_0 represent the magnetic flux along line A with and without back iron, respectively. It can be seen that the thickness of the back iron has a negligible impact on the magnetic susceptibility. Hence, it is disregarded in this paper. Additionally, an approximately linear relationship between magnetic susceptibility and distance x_a can be observed in Fig. 9(a). A linear function through fitting this relationship is provided as the first term in the product of Eq. (13). Additionally, Fig. 9(b) demonstrates the effect of upper back iron, with a fixed thickness, on magnetic susceptibility. Notably, the magnetic susceptibility increases as the increase of distance x_a. Despite the variations in distance x_b, a similar parabolic relationship between magnetic susceptibility and distance x_b is observed. Therefore, a quadratic function is employed to characterize this relationship, which is presented as the second term in the product of Eq. (13).

In summary, the existence of back iron can greatly increase the magnetic field generated by PMs. Taking the parameters in Table 1 as example, the final fitting results by curve fitting approach can be expressed as follows

$$\chi_m = (1.14x_a + 55)(1.26x_a^2 + 1.01x_a + 31.5) \quad (13)$$

5. Finite element model for AEC-PTMD

5.1 3D finite element model

The 3D finite element model (FEM) developed in COMSOL Multiphysics software to calculate the magnetic field and the eddy current damping is shown in Fig. 10. The suspension of the AEC-PTMD is ignored since the emphasis in this section is on its eddy current damping. As illustrated in Fig. 10(b), a cylindrical coordinate is linked to the stationary parts (*i.e.*, back irons) of the FEM with an origin at the geometric center of the arc-shaped conductor plate. To add angular velocity to the moving components of the FEM, a second cylindrical coordinate origin is created at the same location, which is linked to the moving parts (*i.e.*, conductor plate). To ensure the convergence of data, a small angular velocity of $\dot{\theta} = 10\frac{\text{rad}}{s}$ is applied to the conductor plate. A frequency-dependent solver is utilized to calculate the eddy current damping, and the damping force can be obtained by integrating the time-mean Lorentz force on the conductor plate. In addition, the magnetic field distribution of the PMs is calculated by using a stationary solver.

5.2 Results analysis

The eddy current damping coefficient can be calculated

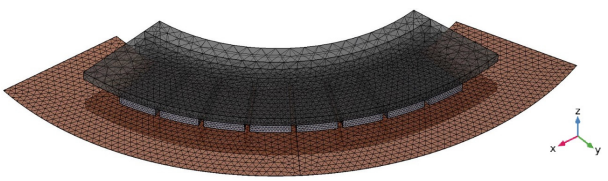

(a) Meshing details of the AEC-PTMD's FEM

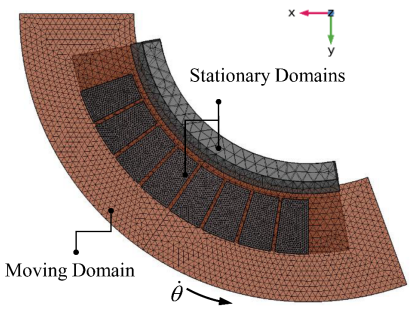

(b) The upper PMs' arrangement and the conductor plate in the XY-planes

Fig. 10 3D FEM of the AEC-PTMD

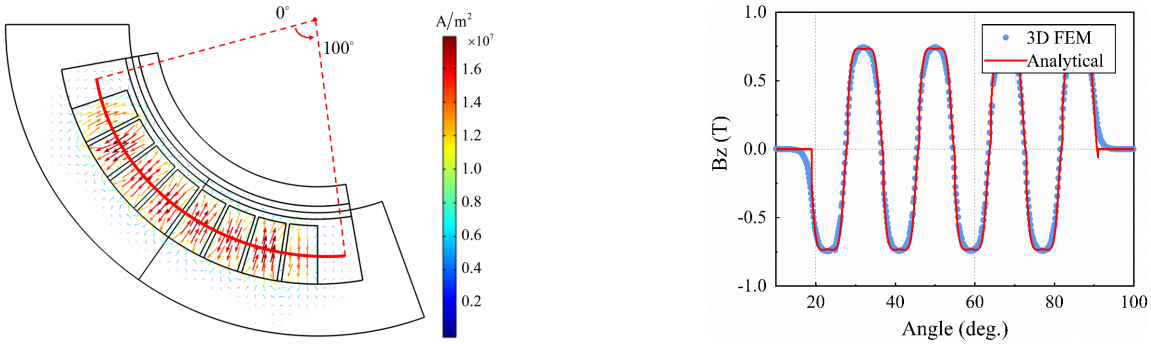

(a) Volume density vector of the eddy currents (b) Magnetic field comparison

Fig. 11 Results of the AEC-PTMD's FEM

by dividing the damping force acting on the conductor plate along the tangent direction by its tangential velocity. It should be noted that the tangential velocity on the conductor plate varies at different positions of the conductor plate, and the distribution law of Lorentz force is similar. Therefore, the damping force and tangential velocity is calculated by integral form on the conductor plate. The eddy current damping coefficient can be expressed as

$$C_{FEM} = \frac{\left(F_{Lx}\, sin\left(\text{atan}\frac{y}{x}\right) - F_{Ly}\, cos\left(\text{atan}\frac{y}{x}\right)\right)}{\dot{\theta}\sqrt{x^2+y^2}} \frac{\theta_t}{360} \quad (14)$$

where F_{Lx}, F_{Ly} are the x and y components of the Lorentz force on the surface of the conductor plate and (x, y) are the position of this force.

The results of the AEC-PTMD's FEM are displayed in Fig. 11. Fig. 11(a) shows that the eddy current is mainly distributed in the projection plane of PMs. Moreover, it can be seen that the eddy current is uniformly distributed throughout the conductor plate, while its magnitude at the edges is close to zero. Fig. 11(b) displays a comparison between the magnetic field on the surface of the conductor plate obtained from the analytical expressions and the FEM simulation, which shows a strong agreement between both. The compared magnetic field in Fig. 11(b) is taken from the location marked by red line in Fig. 11(a). In other words, this comparison confirms the accuracy of the analytical expressions derived earlier.

6. Experimental study

In this section, laboratory experiments of AEC-PTMD prototype with different thickness of the conductor plate is performed. The analytical method and finite element simulations are used to evaluate these conditions, and the results are compared to the experimental results.

6.1 Test method

The aforementioned AEC-PTMD prototype is employed to perform the test. The conductor plate of this prototype can be easily replaceable, on the contrary, the back iron and PMs are fixed. The experimental setup of the AEC-PTMD prototype is displayed in Fig. 12. The apparatus used in this

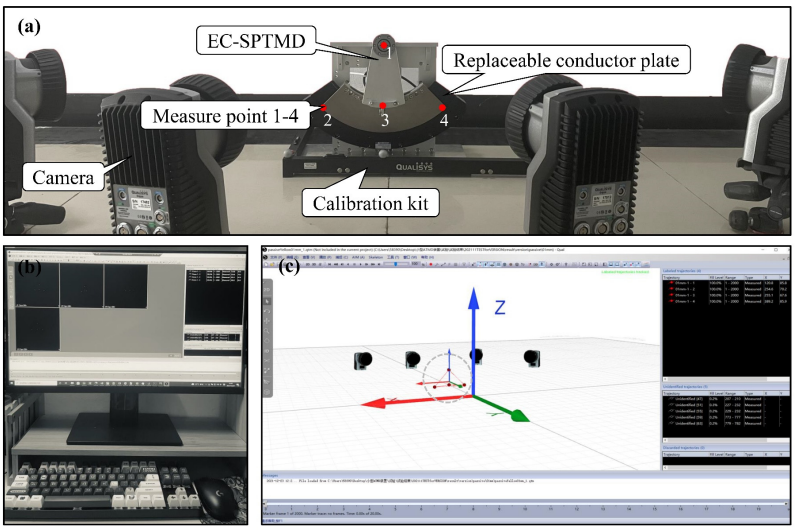

Fig. 12 Experimental system for characterization testing of the AEC-PTMD prototype: (a) overview of tests; (b) data acquisition system; (c) Qualisys Track Manager software

experiment included a motion capture system (QUALISYS Corporation) with four cameras to film the movement of AEC-PTMD prototype, four measure points installed on the prototype with the center of rotation at fixed point 1, a Qualisys Track Manager (QTM) software to acquire data with a 100 Hz sampling rate to record the time histories of 6-DOF motion of prototype, and a PC to process the output data. Before charactering the prototype, the calibration kit is firstly used to determine the coordinate plane and calibrate the motion length. The four points are refined as a rigid body, as shown in Fig. 12(c), This allows for the determination of the angle trajectory of the mass block from the QTM data.

6.2 Results comparison

To evaluate the effectiveness of the proposed AEC-PTMD and the accuracy of the analytical and FEM results, a series of tests involving different thickness of the conductor plate are performed. The experimental eddy current can be calculated as follows

$$C_t = 2m(\omega_t\zeta_t - \omega_0\zeta_0) \tag{15}$$

where m is the mass of AEC-PTMD, ω_0, ω_t are the natural frequency of AEC-PTMD without or with conductor plate, respectively. Meanwhile, ζ_0, ζ_t are the corresponding damping ratios.

The time history of angular trajectory and its frequency spectrum of the AEC-PTMD prototype under different conditions are given in Fig. 13. To obtain a more accurate natural frequency, a chirp-Z transform approach is used to refine the frequency band [0.6, 1.6] Hz. Meanwhile, Table 2 presents a comparison of the eddy current damping of the prototype calculated by analytical expressions, FEM, and experiments.

Compared Fig. 13(a) to Figs. 13(b)-(c), it can be seen that the attenuation of the angular trajectory is greatly reduced with the presence of eddy current damping. The natural frequency of the AEC-PTMD prototype is decreased with thickness of conductor plate increased, which may be attributed to the component of the damping force in the direction of gravity. Therefore, it is important to ensure consistency between the frequency design value and the actual value of the AEC-PTMD prototype. This ensures that the device can effectively perform its intended function when it is designed and implemented.

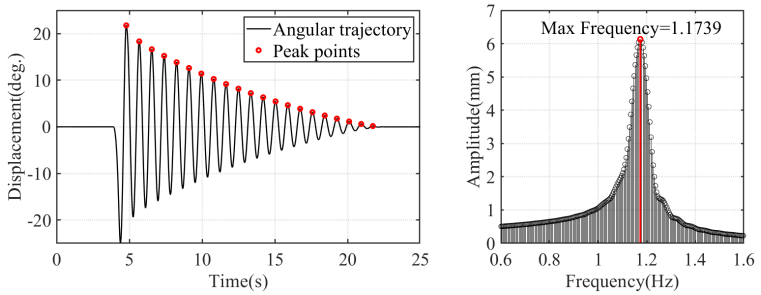

(a) AEC-PTMD prototype without conductor plate

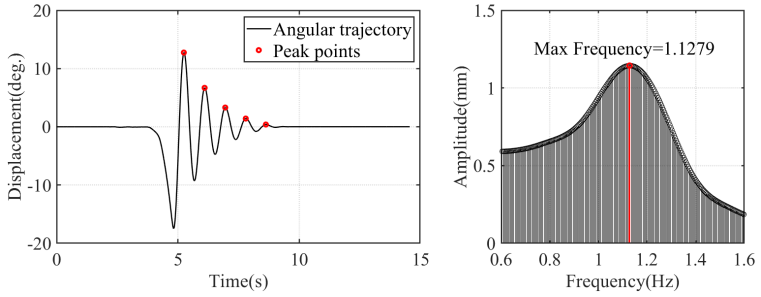

(b) AEC-PTMD prototype with conductor plate of 0.1mm thickness

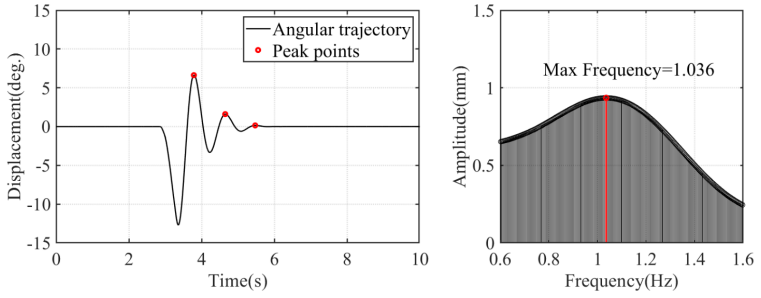

(c) AEC-PTMD prototype with conductor plate of 0.2mm thickness

Fig. 13 Experimental results of angular trajectory and its frequency spectrum for the AEC-PTMD prototype

Table 2 Comparison of eddy current damping coefficient calculation results (Unit: N/m·s)

Symbol	Experiments C_t	FEM C_{FEM}	Analytical results C_a
Y-01mm	0.710	0.636	0.665
Y-02mm	1.417	1.271	1.332
Y-03mm	—	1.907	1.998
Y-04mm	—	2.543	2.665
Y-05mm	3.280	3.183	3.234

In Table 2, the label 'Y-01mm' represents a conductor plate made of yellow brass with a thickness of 0.1 mm, and other labels are similar. It can be seen that there is little difference between the three results, and the analytical results are relatively conservative in comparison to experimental results. The eddy current damping increases with the thickness of conductor plate increases, meanwhile, an approximately linear relationship between both can be observed.

7. Conclusions

In this study, a novel AEC-PTMD with constant eddy current damping is developed, and a small-scaled prototype is subsequently fabricated, modelled and tested. The new configuration of AEC-PTMD guarantees its eddy current damping remains constant during operation. Meanwhile, the assembly feature of the AEC-PTMD makes it easy to achieve the requirement of arbitrary damping.

The analytical expressions derived for the arc-shaped PM accurately calculate the magnetic flux distribution. Meanwhile, the effect of ferromagnetic media on the magnetic field is also studied and modelled by a high-order function. On this basis, the eddy current damping is calculated, which is in good agreement both FEM's and experimental results, with the analytical approach being relatively conservative but more effective for primary design. Overall, this research provides important insights for the design and optimization of AEC-PTMD systems.

Acknowledgments

The research described in this paper was financially supported by the National Natural Science Foundation of China under Grant No. 51921006.

References

Amezquita-Sanchez, J.P., Dominguez-Gonzalez, A., Sedaghati, R., Romero-Troncoso, R.J. and Osornio-Rios, R.A. (2014), "Vibration control on smart civil structures: A review", *Mech. Adv. Mater. Struct.*, **21**(1), 23-38. https://doi.org/10.1080/15376494.2012.677103

Ao, W.K. and Reynolds, P. (2019), "Evaluation of eddy current damper for vibration control of a frame structure", *J. Phys. Commun.*, **3**(5), 055013. https://doi.org/10.1088/2399-6528/ab1deb

COMSOL Inc. (2013), http://www.comsol.com.

Contreras, M.T., Pasala, D.T. and Nagarajaiah, S. (2014), "Adaptive length SMA pendulum smart tuned mass damper performance in the presence of real time primary system stiffness change", *Smart Struct. Syst., Int. J.*, **13**(2), 219-233. http://doi.org/10.12989/sss.2014.13.2.219

Diez-Jimenez, E., Rizzo, R., Gómez-García, M.J. and Corral-Abad, E. (2019), "Review of passive electromagnetic devices for vibration damping and isolation", *Shock Vib.*, Article ID 1250707. https://doi.org/10.1155/2019/1250707

Domenico, D.D. and Ricciardi, G. (2018), "Optimal design and seismic performance of tuned mass damper inerter (TMDI) for structures with nonlinear base isolation systems", *Earthq. Eng. Struct. D.*, **47**(12), 2539-2560. https://doi.org/10.1002/eqe.3098

Domizio, M., Ambrosini, D. and Curadelli, O. (2015), "Performance of TMDs on nonlinear structures subjected to near-fault earthquakes", *Smart Mater. Struct.*, **16**(4), 725-742. http://dx.doi.org/10.12989/sss.2015.16.4.725

Ebrahimi, B., Khamesee, M.B. and Golnaraghi, F. (2009), "Eddy current damper feasibility in automobile suspension: modeling, simulation and testing", *Smart Mater. Struct.*, **18**(1), 015017. http://doi.org/10.1088/0964-1726/18/1/015017

Elias, S. and Matsagar, V. (2017), "Research developments in vibration control of structures using passive tuned mass dampers", *Annual Review Control*, **44**, 129-156. https://doi.org/10.1016/j.arcontrol.2017.09.015

Gerges, R. and Vickery, B. (2005), "Optimum design of pendulum type tuned mass dampers", *Struct. Design Tall Spec. Build.*, **14**(4), 353–368. https://doi.org/10.1002/tal.273

Gou, X.F, Yang, Y. and Zheng, X.J. (2004), "Analytic expression of magnetic field distribution of rectangular permanent magnets", *Appl. Math. Mech.*, **25**(3), 297-306. https://doi.org/10.1007/bf02437333

Haus, H.A., Melcher, J.R., Zahn, M. and Silva, M.L. (1989), *Electromagnetic Fields and Energy*, Prentice Hall, NJ, USA.

Korkmaz, S. (2011), "A review of active structural control: challenges for engineering informatics", *Comput. Struct.*, **89**, 2113-2132. https://doi.org/10.1016/j.compstruc.2011.07.010

Lenggana, B.W., Ubaidillah, U., Imaduddin, F., Choi, S.B., Purwana, Y.M. and Harjana, H. (2021), "Review of magnetorheological damping systems on a seismic building", *Appl. Sci.*, **11**(19), 9339. https://doi.org/10.3390/app11199339

Li, J.Y., Zhu, S. and Shen, J. (2019), "Enhance the damping density of eddy current and electromagnetic dampers", *Smart Struct. Syst., Int. J.*, **24**(1), 15-26. https://doi.org/10.12989/sss.2019.24.1.015

Lu, X.L., Zhang, Q., Weng D.G., Zhou, Z.G., Wang, S.S., Mahin, S.A., Ding, S.W. and Qian, F. (2016), "Improving performance of a super tall building using a new eddy-current tuned mass damper", *Struct. Control Health Monitor.*, **24**(3), e1882. https://doi.org/10.1002/stc.1882

Matta, E. (2019), "A novel bidirectional pendulum tuned mass damper using variable homogeneous friction to achieve amplitude-independent control", *Earthq. Eng. Struct. D.*, **48**(6), 653-677. https://doi.org/10.1002/eqe.3153

Mehrtash, M. and Khamesee, M.B. (2013), "Modeling and analysis of eddy-current damping effect in horizontal motions for a high-precision magnetic navigation platform", *IEEE Trans. Magnet.*, **49**(8), 4801-4810. http://doi.org/10.1109/TMAG.2013.2245675

Mohanta, R.K., Chelliah, T.R., Allamsetty, S., Akula, A. and Ghosh, R. (2017), "Sources of vibration and their treatment in hydro power stations-A review", *Eng. Sci. Technol.*, **20**(2), 637-648. https://doi.org/10.1016/j.jestch.2016.11.004

Nagarajaiah, S. (2009), "Adaptive passive, semiactive, smart tuned

mass dampers: identification and control using empirical mode decomposition, Hilbert transform, and short-term Fourier transform", *Struct. Control Health Monitor.*, **16**(7-8), 800-841. https://doi.org/10.1002/stc.349

Niu, H.W., Chen, Z.Q., Hua, X.G. and Zhang, W.Z. (2018), "Mitigation of wind-induced vibrations of bridge hangers using tuned mass dampers with eddy current damping", *Smart Struct. Syst., Int. J.*, **22**(6), 727-741. https://doi.org/10.12989/sss.2018.22.6.727

Ou, J.P. (2003), *Structural vibration control: active, semi-active and intelligent control*, Science Press, Beijing, China. [in Chinese]

Pasala, D.T. and Nagarajaiah, S. (2014), "Adaptive-length pendulum smart tuned mass damper using shape-memory-alloy wire for tuning period in real time", *Smart Struct. Syst., Int. J.*, **13**(2), 219-233. http://dx.doi.org/10.12989/sss.2014.13.2.203

Pluk, K.J.W., Beek, T.A., Jansen, J.W. and Lomonova, E.A. (2014), "Modeling and measurements on a finite rectangular conducting plate in an eddy current damper", *IEEE Transact. Industr. Elecrtron.*, **61**(8), 4061-4072. http://doi.org/10.1109/TIE.2013.2279364

Roffel, A., Narasimhan, S. and Haskett, T. (2013), "Performance of Pendulum Tuned Mass Dampers in Reducing the Responses of Flexible Structures", *J. Struct. Eng.*, **139**(12), 04013019. https://doi.org/10.1061/(ASCE)ST.1943-541X.0000797

Shi, W.X., Wang, L.K. and Lu, Z. (2017), "Study on self-adjustable tuned mass damper with variable mass", *Struct. Control Health Monitor.*, **25**(3), e2114. https://doi.org/10.1002/stc.2114

Sodano, H.A. and Inman, D.J. (2008), "Modeling of a new active eddy current vibration control system", *J. Dyn. Syst.*, **130**(2), 021009. https://doi.org/10.1115/1.2837436

Sodano, H.A., Bae, J.S., Inman, D.J. and Belvin, W.K. (2005), "Concept and model of eddy current damper for vibration suppression of a beam", *J. Sound Vib.*, **288**(4), 1177-1196. https://doi.org/10.1016/j.jsv.2005.01.016

Sun, C. and Jahangiri, V. (2018), "Bi-directional vibration control of offshore wind turbines using a 3D pendulum tuned mass damper", *Mech. Syst. Signal Pr.*, **105**, 338-360. https://doi.org/10.1016/j.ymssp.2017.12.011

Wang, J.F. and Lin, C.C. (2015), "Extracting parameters of TMD and primary structure from the combined system responses", *Smart Struct. Syst., Int. J.*, **16**(4), 937-960. http://doi.org/10.12989/sss.2015.16.5.937

Wang, Z.H., Chen, Z.Q. and Wang, J.H. (2012), "Feasibility study of a large-scale tuned mass damper with eddy current damping mechanism", *Earthq. Eng. Eng. Vib.*, **11**(3), 391-401. https://doi.org/10.1007/s11803-012-0129-x

Wang, L.L., Nagarajaiah, S., Shi, W.X. and Zhou, Y. (2020), "Study on adaptive-passive eddy current pendulum tuned mass damper for wind-induced vibration control", *Struct. Design Tall Spec. Build.*, **29**(15), e1793. https://doi.org/10.1002/tal.1793

Weber, F. and Maslanka, M. (2012), "Frequency and damping adaptation of a TMD with controlled MR damper", *Smart Mater. Struct.*, **21**(1), 055011. http://doi.org/10.1088/0964-1726/20/1/015012

Weber, F., Boston, C. and Maslanka, M. (2011), "An adaptive tuned mass damper based on the emulation of positive and negative stiffness with an MR damper", *Smart Mater. Struct.*, **20**(1), 015012. http://doi.org/10.1088/0964-1726/20/1/015012

Xu, H.B., Zhang, C.W., Li H. and Ou, J.P. (2014), "Real-time hybrid simulation approach for performance validation of structural active control systems: a linear motor actuator based active mass driver case study", *Struct. Control Health Monitor.*, **21**(4), 574-589. https://doi.org/10.1002/stc.1585

Zhang, H.Y., Chen, Z.Q., Hua, X.G., Huang, Z.W. and Niu, H.W. (2020), "Design and dynamic characterization of a large-scale eddy current damper with enhanced performance for vibration control", *Mech. Syst. Signal Pr.*, **145**(3), 106879. https://doi.org/10.1016/j.ymssp.2020.106879

Zhong, T.F., Feng, X., Zhang, Y. and Zhou, J. (2022), "Experimental study on the effect of EC-TMD on the vibration control of plant structure of PSPPs", *Smart Struct. Syst., Int. J.*, **29**(3), 457-473. https://doi.org/10.12989/sss.2022.29.3.457

Zhu, H.P., Li, Y.M., Shen, W.N. and Zhu, S.Y. (2019), "Mechanical and energy-harvesting model for electromagnetic inertial mass dampers", *Mech. Syst. Signal Pr.*, **120**, 203-220. https://doi.org/10.1016/j.ymssp.2018.10.023

Zuo, L., Chen, X.M. and Nayfeh, S. (2011), "Design and analysis of a new type of electromagnetic damper with increased energy density", *J. Vib. Acoust.*, **133**(4), 041006. https://doi.org/10.1115/1.4003407